Numerical analyses of coupled thermal-hydraulic-mechanical-chemical processes for estimating permeability change in fractured rock induced by alkaline solution

Sho Ogata*, Osaka University, Suita, 565-0871, JAPAN

Hideaki Yasuhara, Ehime University, Matsuyama, 790-8577, JAPAN

Naoki Kinoshita, Ehime University, Matsuyama, 790-8577, JAPAN

Toru Inui, Osaka University, Suita, 565-0871, JAPAN

Eita Nishira, Osaka University, Suita, 565-0871, JAPAN

Kiyoshi Kishida, Kyoto University, Kyoto, 615-8530, JAPAN

*Corresponding author, E-mail address: ogata@civil.eng-osaka-u.ac.jp

1 Introduction

When discussing the stability of geological repositories containing high-level radioactive waste (HLW), the long-term evolution of the hydraulic behavior of a rock mass that works as a natural barrier to the transport of radionuclides must be numerically predicted [1]. The hydraulic behavior within the natural barrier may be governed by the permeability of the multiple fractures that are generated when the cavity is excavated for the disposal of the HLW [2-8]. In addition, after the disposal of the HLW into the excavated cavity, the permeability of the fractures will be influenced by the coupled processes of various physical/chemical phenomena. These processes include the heat transfer from the waste package, the groundwater flow, and the reactive transport with geochemical reactions between the rock minerals and the groundwater (e.g., dissolution/precipitation of the rock minerals) [9, 10]. Therefore, for evaluating the long-term performance of a natural barrier, a coupled numerical model that can comprehensively explain the coupled Thermal-Hydraulic-Mechanical-Chemical (THMC) processes within fractured rock is required. In particular, among the coupled processes, the geochemical reactions, such as the pressure solution at the contacting asperities and the free-face dissolution/precipitation at the free surface within rock fractures, have a non-negligible impact on the alteration of the fracture

37 geometry/permeability over the long duration [11-21]. Several studies [13-15] have
38 confirmed that the pressure solution at the contacting asperities within fractures may bring
39 about the permeability evolution of the fractured rock by several orders of magnitude over
40 a long period. As these geochemical reactions depend on the temperature, stress, and
41 chemical conditions of the groundwater (e.g., solute concentration and pH value) [11-21],
42 they might be affected by the inflow of the alkaline cement solution from an artificial
43 barrier, which can be expected in the actual environments where HLW is isolated [1].
44 Although many numerical works employing coupled models have been performed [22-
45 35], the influence of the above-mentioned inflow of the alkaline cement solution on the
46 chemically induced change in permeability of the fractures initiated/propagated during
47 cavity excavation has not yet been quantitatively evaluated.

48 For example, Taron et al. [34] and Renchao et al. [35] presented coupled THMC
49 numerical simulations considering the dissolution/precipitation of multi-minerals
50 depending on the temperature, stress, and chemical conditions of the fluid. However, their
51 simulations can only describe the changes in permeability in the existing rock fractures
52 because no consideration was given to the process of fracture generation. Meanwhile,
53 although Liu et al. [36] proposed a coupled THMC numerical analysis considering the
54 evolution of rock damage and permeability, caused by hydraulic-chemical erosion and

55 depending on the pH values, the pressure solution was not incorporated into the analysis.
56 Ogata et al. [37] predicted a series of rock permeability evolution processes in a natural
57 barrier within a geological repository of HLW, from fracture generation to subsequent
58 sealing, which results from the pressure solution and free-face precipitation by using a
59 developed coupled THMC numerical model, denoted as the interfaces packaging
60 problem-solving algorithm under coupled conditions, *IPSACC*. However, this numerical
61 prediction does not consider the inflow of the alkaline cement solution from an artificial
62 barrier because the influence of the pH values of the groundwater on geochemical
63 reactions is not incorporated in the model. Besides, the model does not take into account
64 the geochemical reactions within rock matrix, which is also necessary to precisely address
65 the geochemical processes in fractured rock.
66 In this study, our coupled THMC numerical model, *IPSACC*, which is improved by
67 adding the pH dependence and reaction scheme within rock matrix in geochemical
68 processes, was applied to predict the long-term permeability alteration of a natural barrier
69 composed of crystalline rocks within a repository of HLW under subsurface conditions,
70 including the inflow of the alkaline cement solution from an artificial barrier. Performing
71 the numerical investigation of the impacts of the inflow of the alkaline cement solution
72 on the chemically induced change in permeability of the fractured rock is a novelty of this

work.

2 Numerical model

2.1 Model description

The coupled THMC numerical model, introduced in this study, is capable of addressing the interactions of numerous physical/chemical phenomena, such as the heat transfer from the waste package, the fluid flow, the fracture initiation/propagation within the rocks, solute transport, and the dissolution/precipitation of the multi-minerals in the pore fluid. A natural barrier composed of crystalline rock is the target of the numerical simulation for this model, while the phenomena in the artificial barrier are not considered. In the model, the interactions between the T, H, M, D, and C components were taken into account, as illustrated in **Fig. 1**. The model was established by making some improvements to our previous model [37]. The most important improvement was to expand the model and its realm of implementation for computing the laws of geochemical reactions depending on the pH distribution in the fractured rock. This improvement will enable consideration of the influence of the inflow of the alkaline cement solution from an artificial barrier, and will be helpful for analyzing and understanding the controlling factors for the long-term permeability evolution of fractured rock under the expected environment of geological repositories of HLW. The other major improvement was to add consideration of the geochemical reactions in the rock matrix, while the previous model [37]

considered only the reactions in the rock fractures. Above-mentioned improvements are expressed as blue letters in **Fig. 1**.

2.2 Governing equations

The coupled THMC processes addressed in the proposed model are computed using some governing equations, including Darcy's law and the conservation law of water mass, the heat transfer equation, the poroelastic theory, the scalar damage model, the solute transport equation, and the law of mineral dissolution/precipitation. In this section, these governing equations are introduced in order.

2.2.1 Mechanical equilibrium

The target material for the model is assumed as a saturated crystalline rock, indicating the behavior of an elastic body. Regarding the mechanical behavior, and assuming the plane strain condition, the stress/deformation distributions in the rock mass are evaluated by the quasi-static equilibrium equation and the typical Hooke's law, including the effect of the pore pressure and thermal expansion based on the poroelastic theory, as follows:

$$-\nabla\cdot\boldsymbol{\sigma}=\boldsymbol{F}_v, \tag{1}$$

$$\boldsymbol{\sigma}=C:(\boldsymbol{\varepsilon}-\boldsymbol{\alpha}_T\Delta T)+\alpha_B\, p\boldsymbol{I}, \tag{2}$$

where $\boldsymbol{\sigma}$ [Pa] is the stress tensor, $\boldsymbol{F}_v$ [Pa m^{-1}] is the body force, $\boldsymbol{C}$ [Pa] is the elasticity tensor, p [Pa] is the pore pressure, $\boldsymbol{\varepsilon}$ [-] is the strain tensor, $\boldsymbol{\alpha}_T$ [K^{-1}] is the thermal expansion coefficient of the solid,

107 T [K] is the temperature, α_B [-] is the Biot-Willis coefficient, and $\boldsymbol{I}$ [-] is the identity tensor.

108

109 ### 2.2.2 Damage evolution

110 The initiation and propagation of rock fractures within a rock mass are computed by the isotropic
111 scalar damage model which has been applied in a lot of simulations for fracture evolution [28-30, 39-
112 44]. In the current model, the behavior of the damage evolution is expressed by a formulation proposed
113 previously by Tang (1997) [39] and Zhu and Tang (2004) [41]. As depicted in **Fig. 2,** the elastic
114 damage constitutive law for an element under the conditions of uniaxial tension and uniaxial
115 compression is utilized to simulate the rock fracturing process. It is noted that the tensile stress and
116 the compressive stress are set to be negative stress and positive stress, respectively. Damage in tension
117 or in shear begins to progress when the stress state of an element reaches the maximum tensile stress
118 criterion or the Mohr-Coulomb failure criterion, respectively, given by

119
$$\begin{cases} F_t \equiv -\sigma'_3 - f_{t0} = 0 \\ F_s \equiv \sigma'_1 - \dfrac{1+\sin\theta}{1-\sin\theta}\sigma'_3 - f_{c0} = 0 \end{cases}, \tag{3}$$

120 where F_t and F_s are the two damage threshold functions for tensile damage and shear damage,
121 respectively, σ'_1 (= $\sigma_1 - \alpha_B p$) [Pa] and σ'_3 (= $\sigma_3 - \alpha_B p$) [Pa] are the maximum and minimum
122 principal effective stresses, respectively, f_{t0} [Pa] and f_{c0} [Pa] are the uniaxial tensile strength and
123 uniaxial compressive strength, respectively, and θ [°] is the internal friction angle.

In the isotropic damage theory, the elastic modulus E of the damaged rock monotonically decreases with the progress of the damage, as follows:

$$E = (1 - D) E_0 , \tag{4}$$

where E_0 [Pa] and E [Pa] are the elastic moduli of the rock before and after the initiation of damage, respectively, and D [-] is the scalar damage variable that changes from 0 to 1.0 and expresses the degree of damage to the targeted material. D becomes 0 when no damage occurs and 1 when complete damage occurs. In the current work, the zone where damage has progressed considerably ($D > D_{cr}$ = 0.8) is treated as a mesoscopic fracture. And, this mesoscopic fracture (damage zone: $D>D_{cr}$) is defined as a "fracture", while a macroscopic fracture, composed of the calescence of multiple mesoscopic fractures, is generally called a fracture. Meanwhile, the zone where $D \le D_{cr}$ is treated as the rock matrix zone. Damage variable D is computed by strain, as follows [31].

According to the failure criteria of Eq. (3) and the constitutive relationship shown in **Fig. 2**, damage variable D is computed as follows:

$$D = \begin{cases} 0 & F_t < 0 \ \ and \ \ F_s < 0 \\ 1 - \dfrac{\eta \varepsilon_{t0}}{\varepsilon_t} & F_t = 0 \quad and \quad \Delta F_t > 0 \\ 1 - \dfrac{\eta \varepsilon_{c0}}{\varepsilon_c} & F_s = 0 \quad and \quad \Delta F_s > 0 \end{cases} , \tag{5}$$

$$\varepsilon_t = \frac{1}{1+v}\left[\varepsilon_3 + \frac{v}{1-2v} \varepsilon_v \right], \tag{6}$$

$$\varepsilon_c = \frac{1}{1+v}\left[\varepsilon_1 + \frac{v}{1-2v}\varepsilon_v\right] - \frac{1+\sin\theta}{1-\sin\theta}\frac{1}{1+v}\left[\varepsilon_3 + \frac{v}{1-2v}\varepsilon_v\right], \quad (7)$$

where ε_{t0} [-] and ε_{c0} [-] are the limit tensile strain and compressive strain, respectively, η [-] is a constant ($\eta = 0.1$), ε_i (i = 1, 2, 3) are the principle strains in the first, second, and third principal stress directions, respectively, ε_v [-] is the volumetric strain, and v [-] is Poisson's ratio.

2.2.3 Characterization of heterogeneity

The heterogeneity of the rock mass is considered by setting the mechanical properties of each element in the calculation domain according to the Weibull distribution, as defined in the following probability density function [46]. Specifically, among the mechanical properties, the heterogeneity is considered in setting the elastic modulus, uniaxial tensile strength, and uniaxial compressive strength [39, 41].

$$f(u) = \frac{m}{u^s}\left(\frac{u}{u^s}\right)^{m-1}\exp\left[-\left(\frac{u}{u^s}\right)^m\right], \quad (8)$$

where u is the mechanical parameter of each element in the calculation domain, such as the strength and the elastic modulus (i.e., $u = E_0, f_{t0}$, and f_{c0}), u^s is the characteristic parameter which is related to the average value of that mechanical parameter (i.e., $u^s = E_0{}^s$, $f_{t0}{}^s$, and $f_{c0}{}^s$), and m [-] is the homogeneity index of the material properties which defines the shape of the distribution function.

The behavior of the groundwater flow within a rock mass is described by the conservation of water mass employing poroelasticity and by assuming the Darcian flow as

$$\rho_w S \frac{\partial p}{\partial t} + \nabla \cdot (\rho_w \boldsymbol{u}) + \rho_w \alpha_B \frac{\partial \varepsilon_v}{\partial t} = f_w , \tag{9}$$

$$\boldsymbol{u} = -\frac{\boldsymbol{k}}{\mu}(\nabla p + \rho_w g \nabla h) , \tag{10}$$

$$S = \frac{\varphi}{K_f} + \frac{(1-\varphi)}{K_s} \tag{11}$$

$$\alpha_B = 1 - \frac{K}{K_s} \tag{12}$$

where ρ_w [kg m^{-3}] is the liquid density, S [Pa^{-1}] is the storage coefficient, $\boldsymbol{u}$ [m s^{-1}] is the liquid velocity tensor, f_w [kg m^{-3} s^{-1}] is the source term for the flow, $\boldsymbol{k}$ [m^2] is the rock permeability tensor, μ [Pa s] is the liquid dynamic viscosity, g [m s^{-2}] is the gravity acceleration, and h [m] is the potential head, φ is the porosity at an arbitrary time, K [Pa] is the bulk modulus of rock, K_f [Pa]is bulk modulus of fluid, and K_s [Pa] is the bulk modulus of solid. The permeability within the rock mass is distinguished by the degree of damage [47], namely,

$$k = \begin{cases} k_0 \dfrac{(1-\varphi_i)^2}{(1-\varphi)^2}\left(\dfrac{\varphi}{\varphi_i}\right)^3 \exp(\alpha_k D) & D \le D_{cr} \\ \dfrac{b_f^{\,2}}{12} & D > D_{cr} \end{cases} , \tag{13}$$

where k_0 [m^2] is the permeability of the undamaged rock, φ_i is the initial porosity, α_k [-] is the damage-permeability effect coefficient, and b_f [m] is the average fracture aperture which is defined

only in the damage zone where $D>D_{cr}$. As shown in Eq. (11), change in permeability of rock matrix due to porosity change is considered by applying the Kozeny-Carman equation [48], while it was not considered in our previous model [37]. The occurrence of a fracture aperture brought about the damage progression, $b_{f,D}$, is expressed as [47]

$$b_{f,D} = \sqrt{12 k_0 \exp(\alpha_k D)} \ , \tag{14}$$

2.2.4 Heat transfer

In the thermal transport process, the temperature field within the rock is determined by solving the following heat transfer equations:

$$(\rho C_p)_{eq} \frac{\partial T}{\partial t} = \nabla \cdot (\boldsymbol{\lambda_{eq}} \nabla T) - \rho_w C_{p,w} \boldsymbol{u} \cdot \nabla T + q_h \ , \tag{15}$$

$$(\rho C_p)_{eq} = (1-\varphi)\, \rho_m C_{p,m} + \varphi\, \rho_w C_{p,w} \ , \tag{16}$$

$$\boldsymbol{\lambda_{eq}} = (1-\varphi)\, \boldsymbol{\lambda_m} + \varphi\, \boldsymbol{\lambda_w} \ , \tag{17}$$

where $(\rho C_p)_{eq}$ [J K^{-1} m^{-3}] is the equilibrium volumetric heat capacity, $C_{p,w}$ [J kg^{-1} K^{-1}] is the heat capacity of the fluid, $\boldsymbol{\lambda_{eq}}$ [W m^{-1} K^{-1}] is the equilibrium thermal conductivity tensor, q_h [W m^{-3}] is the heat source, ρ_m [kg m^{-3}] is the density of the solid, $C_{p,m}$ [J kg^{-1} K^{-1}] is the heat capacity of the solid, and $\boldsymbol{\lambda_m}$ and $\boldsymbol{\lambda_w}$ [W m^{-1} K^{-1}] are the thermal conductivity tensors of the solid and the liquid, respectively.

The thermal conductivity is correlated according to the evolution of damage [30] as

$$\lambda_m = \lambda_{m0} \exp(\alpha_\lambda D) \tag{18}$$

where α_λ [-] is the damage-solid thermal conductivity coefficient, and λ_{m0} [W m^{-1} K^{-1}] is the initial thermal conductivity of the solid without damage.

2.2.5 Reactive transport

The advection-diffusion equation, including the reaction term, is utilized to describe the distribution of solute concentrations. The mechanical dispersion and retardation, brought about by the sorption processes, are not taken into account here.

$$\frac{\partial(c_i \varphi)}{\partial t} + \boldsymbol{u} \cdot \nabla c_i = \nabla \cdot (\boldsymbol{D_{e,i}} \nabla c_i) + r_i, \tag{19}$$

$$\boldsymbol{D_{e,i}} = \varphi \tau \boldsymbol{D_{b,i}}, \tag{20}$$

$$r_i = \sum_j^n v_i R_j, \tag{21}$$

where c_i [mol m^{-3}] is the concentration of solute i, $\boldsymbol{D_{e,i}}$ [m^2 s^{-1}] is the effective diffusion coefficient tensor, $\boldsymbol{D_{b,i}}$ [m^2 s^{-1}] is the diffusion coefficient tensor, τ [-] is the coefficient related to tortuosity (τ = 1.0), r_i [mol m^{-3} s^{-1}] is the source term of solute i, where v_i [-] is the stoichiometry coefficient of solute i, n is the number of rock-forming minerals, and R_j [mol m^{-3} s^{-1}] is the rate of geochemical reactions

for mineral *j*. The dissolution rate constant and diffusion coefficient are controlled by the system and can be defined by an Arrhenius-type equation [49].

$$D_{b,i} = D_{b,i}^{0} \exp(-E_{D,i} / RT), \quad (22)$$

where $D_{b,i}^{0}$ [m^2 s^{-1}] and $E_{D,i}$ [J mol^{-1}] are the pre-exponential factor and the activation energy of the diffusion of solute *i*, respectively, and *R* [J mol^{-1}K^{-1}] is the gas constant.

2.2.6 Geochemical reactions

The geochemical reactions between rock and water include the free-face dissolution/precipitation and the pressure solution. Therefore, the rate of the geochemical reactions for mineral *j*, R_j, is represented as

$$R_j = R_j^{FF} + R_j^{PS}, \quad (23)$$

where R_j^{FF} [mol m^{-3} s^{-1}] is the rate of the free-face dissolution/precipitation of mineral *j* within the rock, and R_j^{PS} [mol m^{-3} s^{-1}] is the rate of the pressure solution of mineral *j* within the rock.

In the current model, geochemical reactions within both fracture and matrix domains are considered. However, based on the equations of the pressure solution law, presented in Yasuhara et al. (2016)[33], it can be inferred that the pressure solution at the grain contacts within the matrix domain may not occur in crystalline rock that has extremely low porosity. Thus, among the reactions within the matrix domain, only free-face dissolution/precipitation is considered, while the pressure solution

is not considered. The equation for the rate of the reactions within the fracture is formulated by setting the geometric model derived by idealizing the arbitrary micro-domain as the representative element of the fracture area (**Fig. 3** [13]). In the proposed model, the greatly damaged zone, where $D>D_{cr}$, is defined as the fracture, while the other zone is assumed as the rock matrix. Consequently, the rates of the free-face dissolution/precipitation in the matrix and fracture domains can be defined by using the damage variable in the following equation. The equations for the matrix and fracture domains are given in Lasaga (1984) [50] and Ogata et al. (2018) [27], respectively.

$$\begin{cases} R_j^{FF} = f_{r,j}\chi_j k_{+,j} A_{geo}(1-Q_j/K_{eq,j}) & D \le D_{cr} \\ R_j^{FF} = 2f_{r,j}\chi_j k_{+,j}(1-Q_j/K_{eq,j})/b_f & D > D_{cr} \end{cases} \tag{24}$$

where $k_{+,j}$ [mol m^{-2} s^{-1}] is the mineral dissolution rate constant of mineral j, χ_j [-] is the volumetric ratio of mineral j, f_r [-] is the roughness factor, which is the ratio of the true (microscopic) surface area over the apparent (geometric) surface area, Q_j [-] is the ionic activity product, $K_{eq,j}$ [-] is the equilibrium constant of mineral j, and A_{geo} [m^2 m^{-3}] is the geometric surface area, which is simply evaluated by the ratio of the surface area of the spherical grain of diameter d over the volume, as follows:

$$A_{geo} = \frac{\pi d^2}{\frac{\pi d^3}{6}} = \frac{6}{d} \tag{25}$$

The rate of the pressure solution for mineral j at the contacting asperities within the fracture is expressed by applying the damage variables, criterions for tension and shear damage, given as [37]

234
$$\begin{cases} R_j^{PS}=0 & D\le D_{cr} \\ R_j^{PS}=\dfrac{3R_c f_{r,j}\chi_j V_{m,j}k_{+,j}}{RTb_f(1-R_{f,c})}\left(\dfrac{\langle\sigma'_3\rangle}{R_{f,c}}-\sigma_c\right) & D>D_{cr}, F_t=0 \\ R_j^{PS}=\dfrac{3R_c f_{r,j}\chi_j V_{m,j}k_{+,j}}{RTb_f(1-R_{f,c})}\left(\dfrac{\langle\sigma'_1\rangle+\langle\sigma'_3\rangle}{R_{f,c}}-\sigma_c\right) & D>D_{cr}, F_s=0 \end{cases}, \quad (26)$$

235 where R_c [-] is the contact-area ratio within the fracture, $V_{m,j}$ [m^3 mol^{-1}] is the molar volume of
236 mineral j, σ_c [pa] is the critical stress, and <> are the Macaulay's brackets. According to Eq. (26), the
237 pressure solution induced by compressive stress does not occur within the tension fracture when
238 $\sigma_3 < 0$, but it should occur when the stress state moves to a compressive state (i.e., $\sigma_3 > 0$).

239 The mineral dissolution rate constants, that are significantly important parameters for realizing the
240 geochemical reaction between the rock-forming minerals and water, are represented by the Arrhenius
241 expression with dependence on temperature and the pH condition (i.e., concentration of H^+ in the pore
242 water), given as [51]

243
$$k_{+,j} = k_{1,j}{a_{H^+}}^{n1} + k_{2,j} + k_{3,j}{a_{H^+}}^{n3}, \quad (27)$$

244
$$k_{i,j} = k_{i,j}^{298.15K}\exp\left[\frac{-E_{i,j}}{R}\left(\frac{1}{T}-\frac{1}{298.15K}\right)\right], \quad (28)$$

245 where $k_{i,j}^{29815K}$ (i = 1, 2, 3) [mol m^{-2} s^{-1}] is the rate constant of mineral j at 298 1.5K (25°C), pH = 0
246 under acid, neutral, and base mechanisms, respectively, $E_{i,j}$ (i = 1, 2, 3) [J mol^{-1}] is the activation
247 energy of mineral j under acid, neutral, and base mechanisms, respectively, a_{H+} is the activity of H^+,
248 and n_1 and n_3 are the dimensionless catalysis constants for the acid and base mechanisms, respectively.

In the current work, the introducing Eq. (27) is an essential improvement from our previous model [37] for examining the influence of pH alterations brought about by the inflow of the alkaline cement solution from artificial barrier on chemically-induced permeability change with time in natural barrier.

2.2.7 Porosity change within rock matrix

The changes in both of matrix porosity and fracture aperture are thought to be related to the structure alteration of the pore space within the rock, while the former was not considered in our previous work [37]. In the current model, the change in porosity is only induced by the geochemical effect. Thus, the porosity of the rock matrix at an arbitrary time is obtained by computing the rate of change in porosity due to the free-face dissolution/precipitation within the rock matrix, as follows:

$$\varphi = \varphi_i + \int \dot{\varphi}^{FF} dt, \tag{29}$$

$$\dot{\varphi}^{FF} = \sum_j^n V_{m,j} R_j^{FF} = \sum_j^n f_{r,j} \chi_j V_{m,j} k_{+,j} A_{geo} (1 - Q_j / K_{eq,j}), \tag{30}$$

where $\dot{\varphi}^{FF}$ is the rate of change in porosity of the free-face dissolution/precipitation within the rock matrix.

2.2.8 Fracture aperture change

The change in the fracture aperture stems from the fracture initiation/propagation and geochemical processes. Therefore, the fracture aperture at arbitrary time *t* is defined by taking account of the aperture brought about by the fracture initiation/propagation and the temporal evolution of the aperture induced by the free-face dissolution/precipitation and pressure solution, as follows:

$$b_f(t) = b_{f,D} + \int \dot{b}_f^{FF}(t)dt + \int \dot{b}_f^{PS}(t)dt \ , \tag{31}$$

$$\dot{b}_f^{FF} = \sum_j^n 2 f_{r,j} \chi_j (1 - R_{f,c}) V_{m,j} k_{+,j} (1 - Q_j / K_{eq,j}) \tag{32}$$

$$\begin{cases} \dot{b}_f^{PS}(t) = \sum_j^n \dfrac{-3 f_{r,j} \chi_j k_{+,j} V_{m,j}^2}{RT} \left(\dfrac{\langle \sigma'_3 \rangle}{R_{f,c}} - \sigma_c \right) & D > D_{cr}, F_t = 0 \\ \dot{b}_f^{PS}(t) = \sum_j^n \dfrac{-3 f_{r,j} \chi_j k_{+,j} V_{m,j}^2}{RT} \left(\dfrac{\langle \sigma'_1 \rangle + \langle \sigma'_3 \rangle}{R_{f,c}} - \sigma_c \right) & D > D_{cr}, F_s = 0 \end{cases} , \tag{33}$$

where $\dot{b}_f^{FF}$ [m s^{-1}] is the rate of change in the fracture aperture by the free-face dissolution/precipitation and $\dot{b}_f^{PS}$ [m s^{-1}] is the rate of change in the fracture aperture by the pressure solution. It may be possible to approximate the correlation between the fracture aperture and the contact-area ratio on the fractures by the following simple representation [14]:

$$b_f(t) = b_{f,r} + (b_{f,D} - b_{f,r}) \exp(-(R_{f,c}(t) - R_{f,cD})/a), \tag{34}$$

where $b_{f,r}$ [m] is the residual fracture aperture, a [-] is a constant, and $R_{f,cD}$ [-] is the contact-area ratio within the fracture when a fracture is generated, which is represented as the following equation based on the theoretical background for damage variable D [52]. The detailed derivation process is explained in the literature [37].

$$R_{f,cD} = 1 - D \ . \tag{35}$$

It is noted that, in the present work, after the fracture initiation/propagation, changes in damage variable D are not considered.

2.2.9 Numerical computing system

The proposed model is implemented into the computing system by linking two numerical tools of COMSOL MULTIPHYSICS, a powerful FEM software package [53], and PHREEQC [54], a computer program that performs various aqueous geochemical calculations. The main feature of the calculation procedure is that it solves the reactive transport process (Eq. (19)) by dividing it into two processes based on a non-iterative sequential split operator approach [55]. One process is the solute transport, which is handled in COMSOL MULTIPHYSICS, and the other process comprises the kinetic geochemical reactions, including the free-face dissolution/precipitation and the pressure solution, which is computed by PHREEQC.

Details on the above-mentioned computing system can be found in the literature [37].

3 Numerical investigations of permeability evolution within natural barrier for geological disposal of HLW

The proposed model was applied to numerical simulations for predicting the long-term permeability alteration in rock that works as a natural barrier within a geological repository of HLW. The environment of the target subsurface in the following simulations was set by referring to the Mizunami area of Gifu, Japan, and the actual data were obtained from relevant literature. In the simulations, the horizontal storage system of radioactive waste, introduced in the scientific and technical report summarizing HLW disposal construction in Japan [1], was assumed. The numerical

300 domain, as illustrated in **Fig. 4**, expresses the natural barrier from depths of 450 m to 550 m from the
301 Earth's surface. The disposal cavity had a depth of 500 m and its domain was discretized into 51064
302 rectangular elements. The canisters of radioactive waste were virtually installed in the cavity as a heat
303 source. The horizontal length of 13.32 m was selected for the numerical domain because it may be
304 one-half of the center-to-center distance of each disposal cavity with a diameter of 2.22 m. The
305 numerical domain was composed of granite with a porosity of 1.12% and a dry density of 2620 kg/m^3 .
306 These physical properties were determined by observing core samples drilled from the target site at a
307 depth of 500 m [56, 57]. Considering the heterogeneity of the mechanical properties in the target rock
308 mass, the elastic modulus and strengths (uniaxial tensile strength and uniaxial compressive strength)
309 were distributed within the domain based on the Weibull distribution, and the other properties were
310 set homogeneously. In the current simulations, firstly, an excavation analysis of the disposal cavity
311 was performed. Subsequently, the long-term prediction of the alteration in permeability was
312 implemented by employing the stress condition and the damage distribution obtained from the
313 excavation analysis as the initial conditions. The parameters used in the simulations are shown in
314 **Table 1**. These parameter values were selected by referring to the literature [14, 28, 41, 43, 49, 56, 57,
315 60~62].

3.1 Numerical analysis of disposal cavity excavation

Through the numerical analysis of the disposal cavity, with a diameter of 2.22 m and a depth of 500 m, shown in **Fig. 4**, the behavior of the fracture initiation/propagation rock was predicted. The characteristic parameters related to the average value of the mechanical properties, distributed by the Weibull distribution (i.e., $f_{t0}{}^{s}$, $f_{c0}{}^{s}$, and $E_0{}^{s}$, (see Eq. (8)), were set to be 5.36 MPa, 159.6 MPa, and 50.3 GPa, respectively. These values are equivalent to the mechanical properties evaluated by the core samples collected in-situ from a depth of 500 m [56, 57]. Employing an appropriate value for homogeneity index m (see Eq. (8)), in the range of 1.2~5.0, as shown in previous studies [41, 43], the value of that parameter was set to be 2.0. Poisson's ratio and the internal friction angle were set to be 0.27 and 52.6°, respectively [56, 57]. The initial stress conditions, given in **Fig. 5**, were approximated from the data obtained from the hydraulic fracturing tests conducted at various depths at the target site, and lateral pressure coefficient K_0 was set to be 1.6704 [63]. The initial pore pressure was equivalent to the hydrostatic pressure at the steady state. In the excavation analysis, the excavated wall was set to be in an undrained condition during the excavation because a short-term excavation was assumed. To simulate the excavation process in this analysis, the internal outward radial pressure applied to the cavity boundary was reduced monotonically by 0.25% per step for 400 steps (**Fig. 5**). The fracturing process (change in distribution of damage variable D) around the disposal cavity during the excavation is depicted in **Fig. 6**. The figure distinguishes the tensile damage from the shear damage by modifying

334 the sign for the damage variable D values in the shear mode to negative (i.e., $0 \leq D \leq 1 \Rightarrow -1 \leq D \leq 0$).
335 Thus, the negative numbers ($-1 \leq D < 0$) express the shear damage (areas with blue color), while the
336 positive ones express the tensile damage (areas with red color). The figure shows that multiple
337 fractures grow vertically around the crown, and that the invert and tensile damage is more remarkable
338 than the shear damage. The shear damage occurs near the tensile damage. The maximum principal
339 stress is further increased by the stress concentration due to the decrease in stiffness (reduction) in the
340 neighboring tensile damage zone which may result in shear failure near the tensile damage.
341

342 ## 3.2 Long-term simulations with THMC coupling

343 The initial conditions were set by employing the physical/chemical properties of the target rock
344 that were updated by the damage state (i.e., elastic modulus, permeability, thermal conductivity,
345 fracture aperture, and contact-area ratio within the fracture) through the excavation analysis.
346 Subsequently, the long-term simulations were performed. These long-term simulations target the
347 coupled THMC phenomena after the disposal of the waste package in the excavated cavity. The target
348 rock was assumed to be composed of five minerals, namely, quartz (50 vol%), k-feldspar (12 vol%),
349 albite (10 vol%), anorthite (20 vol%), and biotite (8.0 vol%). The volumetric ratios of the minerals,
350 χ_j, were given by referring to those evaluated by the XRD analysis with Mizunami granite [14]. The
351 important parameters of the kinetic dissolution rate constants (see Eqs. (24) and (25)) for the minerals

352 considered in the simulations, obtained from Palandri and Kharaka (2004) [51] and Li et al. (2006)
353 [64], are given in **Table 2**. The hydraulic and thermal gradients were set to be 0.01 and 2°C/100 m,
354 respectively [65]. When considering radiation from canisters, time-dependent change T_b(t) outside the
355 buffer material, obtained from the literature [1] (**Fig. 7**), was set at the periphery of the cavity as the
356 boundary conditions. The inflow of the alkaline cement solution from an artificial barrier was virtually
357 considered by setting solute concentration c_{in}, shown in **Table 3**, at the periphery of the cavity as the
358 boundary conditions. The solute concentrations contained in the alkaline cement solution were
359 obtained from the literature [66, 67]. A summary of the boundary/initial conditions used in long-term
360 simulations is shown in **Fig. 8**. The chemical conditions of the groundwater at the initial state,
361 including the solute concentrations and the pH value shown in **Table 4**, were set to be the measured
362 values at the target site at a depth of 500 m [68]. In the present work, the fracture initiation/extension
363 is considered during the excavation process of the disposal cavity; namely, the forming of new
364 fractures after the excavation is not taken into account.

365 In the present work, the long-term predictions were implemented in two different cases. The first case
366 is that which virtually considers the inflow of the alkaline cement solution from an artificial barrier by
367 setting the concentrations shown in **Table 3** at the cavity boundary; it is called the "inflow". The other
368 case is that which excludes the above-mentioned inflow phenomenon; it is called the "no-inflow". The
369 **Fig. 8** shows the boundary/initial conditions utilized in the inflow case. In the no-inflow case, the
370 following Neumann boundary condition is set at the cavity boundary instead of the inlet conditions
371 used in the "inflow" case.

372 $$\frac{\partial c_i}{\partial \boldsymbol{n}} = 0 \ . \qquad (36)$$

373 where $\boldsymbol{n}$ represents the outward normal direction to the targeted boundary.

374 The **c**hanges in the permeability distribution around the cavity with time in the range of 0 – 4.0
375 years, under the no-inflow condition and the inflow condition, are shown in **Fig. 9**. In the figure, the
376 permeability is given by log notation (i.e., $\log_{10}k$). The initial state shown in figure suggests that the
377 permeability in the fractured zone, formed by the cavity excavation, increases to about two orders of
378 magnitude greater than the intact rock zone at the maximum. As shown in the figure, in both cases,
379 the permeability within several fractures eventually decreases with time. This may be because of the
380 geochemical reactions that seal the fracture (i.e., pressure solution and precipitation). The maximum
381 reduction in permeability is about two orders of magnitude and occurs after 0.1 years. The difference
382 in permeability evolution between the two cases cannot be clearly confirmed with the time tracking
383 shown in the figure. On the other hand, within the undamaged zones, the permeability around the
384 cavity remains almost unchanged in both cases.

385 An additional case was computed under the inflow condition, which does not consider the
386 occurrence of the pressure solution, in order to examine which geochemical reaction dominates the
387 permeability reduction within the fractures. Permeability distributions at the initial state and after 10
388 years, predicted in the above-mentioned case, are shown in **Fig. 10**. The figure shows that, in the case
389 which does not involve the pressure solution, the permeability within the fractures is almost unchanged.

390 Thus, the decrease in fracture permeability with time, observed in **Figs. 9,** is mainly controlled by the
391 occurrence of the pressure solution at the contacting asperities within the fractures. A comparison of
392 **Figs. 6 and 9** implies that the fractures where the permeability changes almost coincide with the shear-
393 induced fractures. This is because the driving force of the pressure solution is the compressive stress
394 which does not occur under the tensile stress condition.

395 In order to investigate the difference in permeability evolution within the fractures, by the influence
396 of the inflow of the alkaline solution, the changes in permeability at an early period under the no-
397 inflow and inflow conditions are shown in **Fig. 11**. In figure, the permeability distribution except the
398 rock matrix is extracted to visualize the permeability evolution within the fractures. Note that the
399 permeability is normalized by the initial value of this long-term coupled analyses after the disposal of
400 the waste package. The figure shows that the relatively clear difference in the permeability distribution
401 close to the cavity at 0.001 years between two cases can be confirmed visually, while there is almost
402 no difference after 0.1 years. The distributions of normalized fracture permeability focused near the
403 invert at 0.001 years the no-inflow and inflow conditions are shown in **Fig. 12.** As is apparent from
404 the figure, the progress of permeability reduction under the inflow condition is faster than that under
405 the no-inflow condition. Subsequently, the changes in pH within fractures with time under the no-
406 inflow condition and the inflow condition, are shown in **Fig. 13.** In the figure, it is showed that the pH
407 close to the cavity increases to around 12 due to gradually expansion of the alkaline solution from the

408 cavity boundary with time under the inflow condition, while the pH is around 9.0 under the no-inflow
409 condition. The increase of pH with time within the fractures in both also be affected by the
410 consumption of H^+ ion which is induced by the occurrence of mineral dissolution (e.g., pressure
411 solution). From the **Figs 11~13**, it is confirmed that the difference in the permeability evolution
412 between two cases (no-inflow condition and inflow condition) is significant only in the vicinity of the
413 cavity in the early stage of disposal period and it is brough about by the locally enhancement of
414 pressure solution by increase of the reaction rates depending on the pH value due to expansion of the
415 alkaline solution. The occurrence of these local trend is because of a greatly difference between
416 pressure solution rate and expansion rate of alkaline solution. In the scheme of pressure solution
417 expressed by **Eq. (26)**, the reaction stops at equilibrium when the stress acting on the asperity contacts
418 within the fractures (contact stress) becomes equal to the critical stress. The time-dependent
419 degradation of contact stress to reach critical stress is induced by increase of contact area linked to
420 decrease of fracture aperture as defined by **Eq. (34).** From **Fig. 11**, it can be expected that the rapid
421 aperture reduction within the several fractures, is caused by pressure solution after disposal of waste
422 package and at 0.1 years pressure solution has already stopped within most fractures in both cases.
423 Compared to the progress rate of pressure solution until reaching equilibrium, the expansion rate of
424 alkaline solution from the cavity is sol slow. Thus, the behaviour of the pressure solution within the

425 fractures only close to the cavity where the alkaline solution can reach immediately is influenced by
426 the inflow of the alkaline solution.

427 In order to further verify the above-mentioned insights, the changes in permeability and pH with
428 time under the no-inflow condition and the inflow condition at two specific observation point (points
429 1 and 2, see **Fig. 14**) within the fracture are depicted in **Figs 15** and **16**. As shown in **Fig. 14,** point1 is
430 installed in the vicinity of the cavity boundary, while point2 is set in a place a little away from the
431 cavity boundary. As is apparent from the **Figs 15 and 16,** in the fracture close to the cavity (point1)
432 the difference in permeability reduction is significant in the early period (within first 0.015 years)
433 between no-inflow condition and inflow condition, while there is almost no difference in the fracture
434 at a distance from the cavity (point2). This is because that alkaline solution has reached point1, but
435 has not reached point2 under the inflow condition. At the point2, pH evolution under no-inflow
436 condition is almost same as the one under inflow condition and in both cases, permeability almost
437 ends up in the convergence value within first 0.015 years. That is, at a distance from the cavity, the
438 permeability reduction induced by pressure solution has already completed sooner than the alkaline
439 solution arrives. These results observed at specific points are consistent with the insights expected
440 from **Figs 11~13**.

In order to perform the integrated evaluation of permeability reduction throughout the fracture zone , the spatially integrated permeability reduction is taken over the fracture domain at arbitrary time t, $\sum_{\Omega} \Delta k_f(t)$ [m^4], which is represented as follows:

$$\sum_{\Omega} \Delta k_f(t) = \int_{\Omega} \left[k_{f,i} - k_f(t) \right] dxdy \ . \tag{37}$$

where $k_{f,i}$ [m^2] is the permeability of the fracture domain at the initial condition in this analysis, and Ω is the entire fracture domain. The evolution in the spatially integrated permeability reductions over the fracture domain under no-inflow and inflow conditions is depicted in **Fig. 17**. As is apparent from the figure, in both cases, the amounts of integrated reductions rapidly increase in the early stages of the analysis period. Afterwards, they approach almost equal values. To focus on the difference in rates of reduction between the two cases in more detail, an extract of the early period in **Fig. 17** is shown in **Fig. 18**. This figure shows slight differences in the amounts/rates of reduction affected by the inflow of the alkaline solution, and the differences are a little clear to some extent within the first 0.02 years. Much of the difference may have been brought about by the enhancement of the pressure solution only close to the cavity due to the expansion of the alkaline solution.

4 Conclusion

In order to examine the impact of the inflow of the alkaline cement solution on the change in permeability over time within the fractured rocks at an actual field, a coupled THMC numerical model, *IPSACC*, that is able to address a series of permeability evolution, from fracture generation to subsequent geochemical creep, has been upgraded by incorporating the dependence of the

461 geochemical reactions on the pH value. Then, the upgraded model was applied to predict the long-
462 term alteration of the permeability in crystalline rock, which is located in geological disposal facilities
463 of HLW. In the numerical predictions, subsurface conditions were assumed that also virtually consider
464 the inflow of the alkaline cement solution from an artificial barrier. The predicted results show that
465 many fractures are generated during the excavation, and that the permeability within the several shear-
466 induced fractures rapidly decreases afterwards with time due to the pressure solution at the contacting
467 asperities of the fractures. The fracture permeability reduction is locally accelerated only in the vicinity
468 of the disposal cavity due to the significant alkalization of the groundwater induced by the inflow of
469 the alkaline component. This is attributed to that the alkaline component cannot spread the fractures
470 except near the disposal cavity before the permeability reduction induced by pressure solution quickly
471 reaches the steady state. Overall, the performed numerical predictions in this work suggests the
472 possibility that the influence of the inflow of the alkaline cement solution from an artificial barrier is
473 spatiotemporally limited and is not dominant on the long-term performance of a natural barrier
474 composed of crystalline rock for delaying the transport of radionuclides.
475
476
477

References

1. Japan Nuclear Cycle Development Institute, 2000: Second Progress Report on Research and Development for the Geological Disposal of HLW in Japan, Supporting Report 2 Repository Design and Engineering Technology, H12: Project to Establish the Scientific and Technical Basis for HLW Disposal in Japan. JNC TN1410 2000-003, IV-139-IV-160 (2000).

2. Aoyagi, K. and Ishii, E.: A Method for Estimating the Highest Potential Hydraulic Conductivity in the Excavation Damaged Zone in Mudstone. Rock Mech. Rock Eng. **52,** 385-401 (2019).

3. Zhang, C-H.: The stress-strain-permeability behaviour of clay rock during damage and recompaction. J. Rock Mech. Geotech. Eng. **8**, 16-26 (2016).

4. Tsang, C-F., Jing, L., Stephansson, O. and Kautsky, F.: The DECOVALEX III project: A summary of activities and-lessons learned. Int. J. Rock Mech. Min. Sci. **42**, 593-610 (2005).

5. Homand-Etienne, F. and Sebaibi, A.: Study of microcracking of the Lac du Bonnet granite. Eurock-ISRM Int. Symp. **2**, 1353-1362 (1996).

6. Souley, M., Homand, F., Peda, S. and Hoxha, D.: Damaged-induced permeability changes in granite: a case example at the URL in Canada. Int. J. Rock Mech. Min. Sci. **38**, 297-310 (2001).

7. Kelsall, PC., Case, JB. and Chabanne, CR.: Evaluation of excavation induced changes in permeability. Int. J. Rock Mech. Min. Sci. **21**, 121-135 (1984).

8. Bauer, C., Homand, F. and Henry, JP.: In situ low permeability pulse test measurements. Int. J. Rock Mech. Min.

Sci. **32**, 357-63 (1995).

9. Tsang, CF., ed.: *Coupled Processes Associated with Nuclear Waste Repositories*. Amsterdam: Elsevier, 2012.

10. Tsang, Y.: Effects of coupled processes on a proposed high-level radioactive waste repository at Yucca Mountain, Nevada. *Geol Soc Am Memorie*. **209**, 363-393 (2012).

11. Polak, A., Elsworth, D., Yasuhara, H., Grader, A. and Halleck, P.: Permeability reduction of a natural fracture under net dissolution by hydrothermal fluids. Geophys. Res. Lett. **30** (20), 2020, doi:10.1029/2003 GL017575 (2003).

12. Polak, A., Elsworth, D., Yasuhara, H., Grader, AS. and Halleck, PM.: Spontaneous switching of permeability changes in a limestone fracture with net dissolution. Water Resour. Res. **40**, W03502, doi:10.1029/ 2003WR002717 (2004).

13. Yasuhara, H., Elsworth, D. and Polak, A.: Evolution of permeability in a natural fracture: the significant role of pressure solution. J. Geophys. Res. **109**, B03204, doi:10.1029/2003JB002663 (2004).

14. Yasuhara, H., Kinoshita, N., Ohfuji, H., Lee, DS., Nakashima, S. and Kishida, K.: Temporal alteration of fracture permeability in granite under hydrothermal conditions and its interpretation by coupled chemo-mechanical model. Appl. Geochem. **26**, 2074-2088 (2011).

15. Yasuhara, H. and Elsworth, D.: A numerical model simulating reactive transport and evolution of fracture permeability. Int. J. Numer. Anal. Methods Geomech. **30**, 1039-1062 (2006).

16. Yasuhara, H., Elsworth, D., Polak, A., Liu, J., Grader, A. and Halleck, P.: Spontaneous permeability switching in

fractures in carbonate: lumped parameter representation of mechanically and chemically mediated dissolution. Transp Porous Media. **65**: 385–409 (2006).

17. Robert, AC., Ehsan, G., Julia, NP. and Nico, P.: Experimental investigation of fracture aperture and permeability change within Enhanced Geothermal Systems. Geothermics. **62**, 12–21(2016).

18. Beeler, MN. and Hickman, SH.: Stress-induced, time-dependent fracture closure at hydrothermal conditions. J. Geophys. Res. **109**(B3): B02211 doi:10.1029/2002JB001782 (2004).

19. Kinoshita, N. and Yasuhara, H.: Evolution of Fracture Permeability in Granite under High Temperature and High Confining Pressure Condition, Journal of MMIJ. **128**, 72-78 (2012).

20. Yasuhara, H., Hashimoto, K. and Kinoshita, N.: Evaluation of Dissolution Equation in Granite Examination by Flow-Through Dissolution Experiment under Temperature and pH conditions Controlled, Journal of MMIJ, 128, 79-85 (2012).

21. Palandri, JL. and Kharaka, YK.: A compilation of rate parameters of mineral-water interaction kinetics for application to geochemical modelling. US Geological Survey open file report 2004–108, USA (2004).

22. Rutqvist, J., Wu, Y-S., Tsang, C-F. and Bodvasson, G.: A modeling approach for analysis of coupled multiphase fluid flow, heat transfer, and deformation in fractured porous rock. Int. J. Rock Mech. Min. Sci. **39**, 429-442 (2002).

23. Suzuki, H., Nakama, S., Fujita, T., Imai, H. and Sazarshi, M.: A long-term THMC assessment on the geochemical behavior of the bentonite buffer. J. Nucl Fuel Cycle. Environ, **19**, 39-50 (2012).

24. Nasir, O., Fall, M. and Evgin, E.: A simulator for modeling of porosity and permeability changes in near field

sedimentary host rocks for nuclear waste under climate changes influences. Tunneling and Underground Space Technology. **42**, 122-135 (2014).

25. Fall, M., Nasir, O. and Nguyen, T. S.: A coupled hydro-mechanical model for simulation of gas migration in host sedimentary rocks for waste repositories. Eng. Geol. **176**, 24-44 (2014).

26. Zhang, R., Yin, X., Winterfeld, P. H. and Wu, Y.-S.: A fully coupled thermal-hydrological-chemical model for CO_2 geological sequestration. J. Nat. Gas Sci. Eng. **28**, 280-304 (2016).

27. Ogata, S., Yasuhara, H., Kinoshita, N., Cheon, DS. and Kishida, K.: Modeling of coupled thermal-hydraulic-mechanical-chemical process for predicting the evolution in permeability and reactive transport behavior within single rock fractures., Int. J. Rock Mech. Min. Sci. **107**, 271-281 (2018).

28. Wei, CH., Zhu, WC. Chen, S. and Ranjith, PG.: A coupled thermal-hydrological-mechanical damage model and its numerical simulations of damage evolution in APSE. Materials. **9**, 841, doi: 10.3390/ma9110841 (2016).

29. Li, LC., Tang, CA., Wang, SY. and Yu, J.: A coupled thermo-hydrologic-mechanical damage model and associated application in a stability analysis on a rock pillar. Tunneling and Underground Space Technology. **34**, 38-53 (2013).

30. Wei, CH., Zhu, WC., Yu, QL., Xu, T. and Jeon, S.: Numerical simulation of excavation damaged zone under coupled thermal-mechanical conditions with varying mechanical parameters. Int. J. Rock Mech. Min. Sci. **75**, 169-181 (2015).

31. Poulet, T., Karrech, A., Lieb, RK., Fisher, L. and Schaubs, P.: Thermal-hydraulic-mechanical-chemical coupling with damage mechanics using ESCRIPTRT and ABAQUAS. Tectonophysics. 124-132 (2013).

32. Marschall, P., Giger, S., Vassiere, DLR., Shao, H., Leung, H., Nussbaum, C., Trick, T., Lanyon, B., Senger, R., Lisjak, A. and Alcolea, A.: Hydro-mechanical evolution of the EDZ as transport path for radionuclides and gas: insights from the Mont Terri rock laboratory (Switzerland). Swiss J. Geosci. **110**, 173-194 (2017).

33. Yasuhara, H., Kinoshita, N., Ogata, S., Cheon, DS. and Kishida, Kiyoshi.: Coupled thermo-hydro-mechanical-chemical modeling by incorporating pressure solution for estimating the evolution of rock permeability, Int. J. Rock Mech. Min. Sci. **86**, 104-114 (2016).

34. Taron, J., Elsworth, D. and Min., KB.: Numerical simulation of thermal-hydrologic-mechanical-chemical processes in deformable fractured porous media. Int. J. Rock Mech. Min. Sci. **46**, 842-854 (2009).

35. Renchao, L., Thomas, N., Hua S., Olaf, K. and Haibing S.: Modeling of Dissolution-Induced Permeability Evolution of a Granite Fracture Under Crustal Conditions. J. Geophys. Res. **123**, 5609-5627 (2018).

36. Weitao, L., Jiyuan, Z., Ruiai, N., Yifan, Z, Baichao, X. and Xi, S.: A Full Coupled Thermal-Hydraulic-Chemical Model for Heterogeneity Rock Damage and Its Application in Predicting Water Inrush. Appl. Sci. 9, 2195; doi:10.3390/app9112195 (2019).

37. Ogata, S., Yasuhara, H., Kinoshita, N. and Kishida, Kiyoshi. : Coupled thermal–hydraulic–mechanical–chemical modeling for permeability evolution of rocks through fracture generation and subsequent sealing, Computational Geosciences, **24**, 1845-1864, https://doi.org/10.1007/s10596-020-09948-3 (2020).

38. Chaojun, F., Mingkun, L., Sheng, L., Haohao, Z., Zheng, Y. and Zheng, L.: A Thermo-Hydro-Mechanical-Chemical Coupling Model and Its application in Acid Fracturing Enhanced Coalbed Methane Recovery

Simulation. Energies. 12, 626; doi:10.3390/en12040626 (2019).

39. Tang, CA.: Numerical simulation on progressive failure leading to collapse and associated seismicity. Int. J. Rock Mech. Min. Sci. **34**, 249-262 (1997).

40. Tang, CA., Liu, H., Lee, KKP., Tsui, Y. and Tham, LG.: Numerical studies of the influence of microstructure on rock failure in uniaxial compression- Part I : effect of heterogeneity. Int. J. Rock Mech. Min. Sci. **37**, 555-569 (2000).

41. Zhu, WC. and Tang, CA.: Micromechanical model for simulating the fracture process of rock. Rock Mech. Rock Eng. **37**, 25-56 (2004).

42. Li, G. and Tang, CA.: A statistical meso-damage mechanical method for modeling trans-scale progressive failure process of rock. Int. J. Rock Mech. Min. Sci. **74**, 133-150 (2015).

43. Liu, HY., Roquete, M., Kou, SQ. and Lindqvist, PA.: Characterization of rock heterogeneity and numerical verification. Eng. Geol. **72**, 89-119 (2004).

44. Wang, SY., Sloan, SW., Scheng, DC., Yang, SQ. and Tang, CA.: Numerical study of failure behavior of pre-cracked rock specimens under conventional triaxial compression. Int. J. Solids Struct. **51**, 1132-1148 (2014).

45. Wang, J., Elsworth, D., Wu, Yu., Liu, Jishan., Zhu, WC. and Liu, Y.: The Influence of Fracturing Fluids on Fracturing Processes: A Comparison Between Water, Oil and SC-CO_2.Rock. Mech. Rock. Eng. **51**, 299-313 (2018).

46. Weibull, W.: A statistical distribution function of wade applicability. J. Appl. Mech. **18**, 293-297 (1951).

47. Zhu, WC., Weu, C., Li, S., Wei, J. and Zhang, M.: Numerical modeling on destress blasting in coal seam for

586 enhancing gas drainage, Int. J. Rock Mech. Min. Sci. **59**, 179-190 (2013).

587 48. Bear, J.: Dynamics of Fluids in Porous Media, Dover Publications. 161-176 (1972)

588 49. Revil, A.: Pervasive pressure-solution transfer: a poro-visco-plastic model. Geophys. Res. Lett. **26**, 255-258

589 (1999).

590 50. Lasaga, AC.: Chemical kinetics of water-rock interactions. J. Geophys. Res. **89**, 4009-4025 (1984).

591 51. Palandri, JL. And Kharaka, YK.: A compilation of application to geochemical modeling. US Geological Survey

592 open file report. 2004-1068 (2004).

593 52. Cocks, A. and Ashby, M.: Intergranular fracture during power-law creep under multiaxial stresses. Metal Science.

594 **14**, 395-402 (1980).

595 53. COMSOL2014：COMSOL MULTIPHYSICS. Version 5.0, Available from www.comsol.com (2004).

596 54. Parkhurst, DL. and Appelo, CAJ.: Description of Input and Examples for PHREEQC Version3-A Computer

597 Program for Speciation, Batch-Reaction, One-Dimensional Transport, and Inverse Geochemical Calculations,

598 Online version availableromhttp://wwwbrr.cr.usgs.gov/projects/GWC_coupled/phreeqc/phreeqc3-html/phreeq-

599 c3.htm.

600 55. Azad, Vj., Li, C., Verba, C., ldeker, JH. and lsgor, OB.: A COMSOL-GEMS interface for modeling coupled

601 reactive-transport geochemical processes. Comput. Geosci-UK. **92**, 79-89 (2016).

602 56. Gohke, M., Horita M., Wakabayashi N. and Nakatani A.: Excavation disturbance analysis based on Crack Tensor

603 Model and Virtual Fracture Model for predicting the rock mass behavior during excavation of shafts and research

galleries at the Mizunami Underground Research Laboratory. JNC TJ7400. 2005-058 (2005).

57. Gohke, M., Horita M., Wakabayashi N. and Nakatani A.: Excavation disturbance analysis based on Crack Tensor Model and Virtual Fracture Model for predicting the rock mass behavior during excavation of shafts and research galleries at the Mizunami Underground Research Laboratory. JNC TJ7400. 2005-058 (2005).

58. Detounay, E. and Cheng, A.H.-D.: Fundament poroelasticity. in Comprehensive Rock Engineering: Principals, Practice and Projects, 2 edited by Hudson, J.A., Pergamon Press, Oxford. 113-171 (1993).

59. Halt, D.J. and Wang., H.F.: Laboratory measurements of a complete set of poroelastic moduli for Brea sandstone and Indiana limestone, J. Geophy. Res., **100**, 17741-17751 (1995).

60. Kosaka, H., Saegusa, H., Onoue, H. and Takeuchi, R.: Study on Hydrogeology on the Mizunami Underground Research Laboratory Project Hydrogeological Modeling and Groundwater Flow Simulation for Planning of Long-term Pumping Test. JAEA-Research, 2010-037 (2011).

61. Sato, T., Taniguchi, W., Fujita, T. and Hasegawa, H.: Data Collection by Literature Survey on Rock Physics Properties in Japan (Ⅱ). JNC TN7400 99-011 (1999).

62. Wang, J., Elsworth, D., Wu, Yu., Liu, J., Zhu W. and Liu, Y.: The Influence of Fracturing Processes: A Comparison Between Water, Oil and SC-CO^2. Rock. Mech. Rock. Eng. DOI 10.1007/s00603-017-1326-8 (2017).

63. Gohke, M., Horita M., Wakabayashi N. and Nakatani A.: Excavation disturbance analysis based on Crack Tensor Model and Virtual Fracture Model for predicting the rock mass behavior during excavation of shafts and research galleries at the Mizunami Underground Research Laboratory. JNC TJ7400. 2005-058 (2004).

64. Li L., Perters CA. and Celia MA.: Upscaling geochemical reaction rates using pore-scale network modeling. Advances in water resources. **29**, 1351-1370 (2006).

65. JNC (Japan Nuclear Cycle Development Institute), 2005: Development and management of the technical knowledge base for the geological disposal of HLW, Summary of the H17 project reports. Vol. 1. Scientific research of deep underground. JNC TN1400 2005-014 (2005) (in Japanese).

66. Suzuki, H., Ito, A., Yoshida, Y., Suyama, T., Kawakami, S., Sasamoto, H. and Yui, M.: Experimental Studies on the Coupled THMC Processes by COUPLE Equipment - Part I -. JNC-TN8400 2003-033 (2004) (in Japanese).

67. Atkinson, A., Hearne J.A. and Knights, C. F.: Aqueous chemistry and thermodynamic modeling of CaO-SiO_2-H_2O gel, AERER12543 (1987).

68. Hayashida, K., Kato, T., Kubota, M., Murakami, H., Amano, Y. and Iwatsuki, T.: Evaluation of hydrogeochemical proceeses provoked by tunnel excavation and closure based on simulated experiment in a mock-up test drift. Chikyukagaku (Gecgemistly). **59**, 55-71 (2018).

640

641 **Table 1** Parameters used in simulation.

Parameter	Value
Homogeneity index of material properties [-] m	2.0 [41, 43]
Characteristic value of elastic modulus [GPa] $E_0{}^s$	50.3 [56,57]
Characteristic value of uniaxial tensile strength [MPa] $f_{t0}{}^s$	5.36 [56,57]
Characteristic value of uniaxial compressive strength [MPa] $f_{c0}{}^s$	159.6 [56,57]
Internal friction angle [º] θ	52.6 [56,57]
Poisson's ratio [-] v	0.27 [56,57]
Bulk modulus of solid [GPa] K_s	40 [58, 59]
Bulk modulus of fluid [GPa] K_f	2.0
Permeability of the undamaged rock [m^2] k_0	1.82×10^{-16} [60]
Initial porosity [%] φ_i	1.12 [56,57]
Initial thermal conductivity of the solid [w m^{-1} K^{-1}] λ_{m0}	3.0 [61]
Heat capacity of the solid [kJ kg^{-1} K^{-1}] $C_{p,m}$	0.8 [61]
Thermal expansion coefficient of solid [K^{-1}] α_T	1.15×10^{-5} [61]
Coefficient that represents the damage-permeability effect [-] α_k	5.0 [62]
Coefficient that represents the damage-solid thermal conductivity [-] α_λ	5.0 [28]
Roughness factor [-] f_r	7.12 [14]
Critical stress [MPa] σ_c	150 [56,57]
Pre-exponential factor of diffusion of solute [m^2 s^{-1}] D_b^0	5.2×10^{-8} [49]
Activation energy of diffusion of solute [kJ mol^{-1}] E_D	13.5 [49]
Constant [-] a	0.04 [14]

642 Note: The bulk modulus of fluid K_f was set to the general value of water and the critical stress σ_c was
643 set to be equivalent to uniaxial compressive strength of target rock.

644

645

646

647

648

649

Table 2 Parameters of kinetic dissolution rate constant [51,63].

Parameter	Quartz	K-feldspar	Anorthite	Albite	Biotite	Amorphous silica
$\log k_1^{298.15K}$		-10.66	-3.50	-10.16	-9.84	
$\log k_2^{298.15K}$	-13.99	-12.56	-9.12	-12.56	-12.55	-12.3
$\log k_3^{298.15K}$		-21.2	-	-15.6	-	
E_1 [kJ/mol]		51.7	16.6	65	22.0	
E_2 [kJ/mol]	87.6	38.0	17.8	69.8	22.0	76.0
E_3 [kJ/mol]		94.1	1.411	71.0	-	
n_1		0.50	-	0.457	0.525	
n_3		-0.823	-	-0.572	-	

Note: The data on the anorthite and other minerals were obtained from Li et al. (2006) [63] and Palandri and Kharaka (2004) [51], respectively.

Table 3 Chemical composition of alkaline cement solution from cavity boundary (Inlet boundary) [64,65].

Initial pore water composition	Value
Al [mol L^{-1}]	1.29×10^{-3}
Ca [mol L^{-1}]	5.35×10^{-3}
K [mol L^{-1}]	5.81×10^{-2}
Na [mol L^{-1}]	3.76×10^{-2}
Si [mol L^{-1}]	1.19×10^{-6}
Mg [mol L^{-1}]	6.08×10^{-9}
pH	13.90

Table 4 Initial chemical composition of groundwater utilized in simulation [66].

Initial pore water composition	Value
Al [mol L^{-1}]	1.9×10^{-6}
Mn [mol L^{-1}]	3.6×10^{-7}
K [mol L^{-1}]	2.0×10^{-5}
Na [mol L^{-1}]	7.8×10^{-3}
Si [mol L^{-1}]	3.0×10^{-4}
Ca [mol L^{-1}]	2.1×10^{-3}
Mg [mol L^{-1}]	6.0×10^{-6}
Fe [mol L^{-1}]	4.0×10^{-5}
F [mol L^{-1}]	3.0×10^{-4}
Cl [mol L^{-1}]	1.2×10^{-2}
S [mol L^{-1}]	5.0×10^{-7}
N [mol L^{-1}]	2.2×10^{-5}
pH	8.59

.

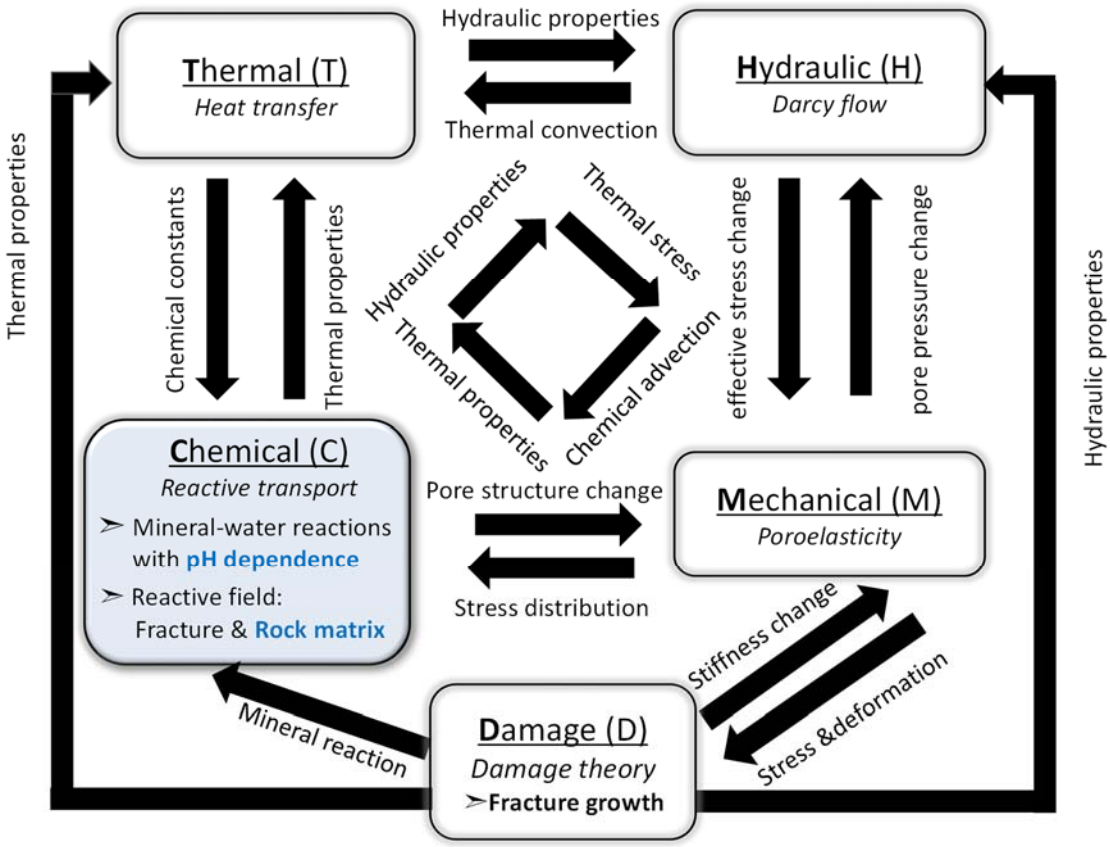

Fig. 1 THMC coupled interactions addressed in the presented model. The component expressed as blue letters were not addressed in our previous model [37]

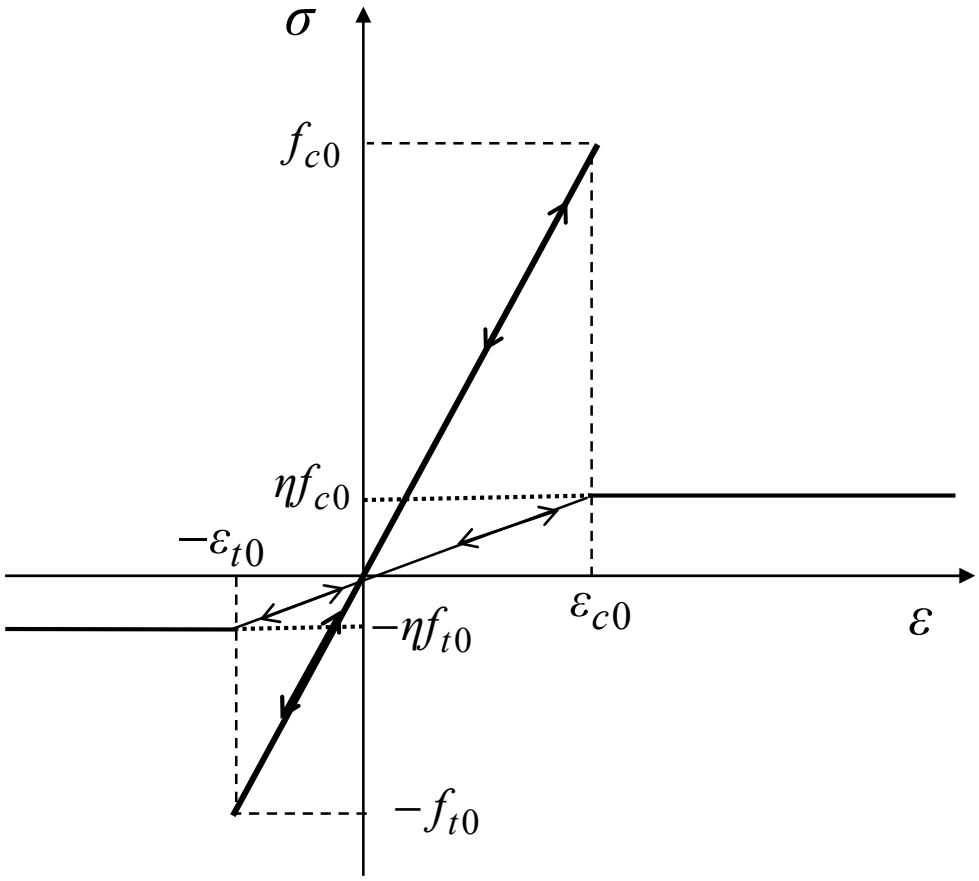

Fig. 2 Constitutive law of damage theory under uniaxial tensile stress and uniaxial compressive stress (illustrated in Li et al., 2013 [29]).

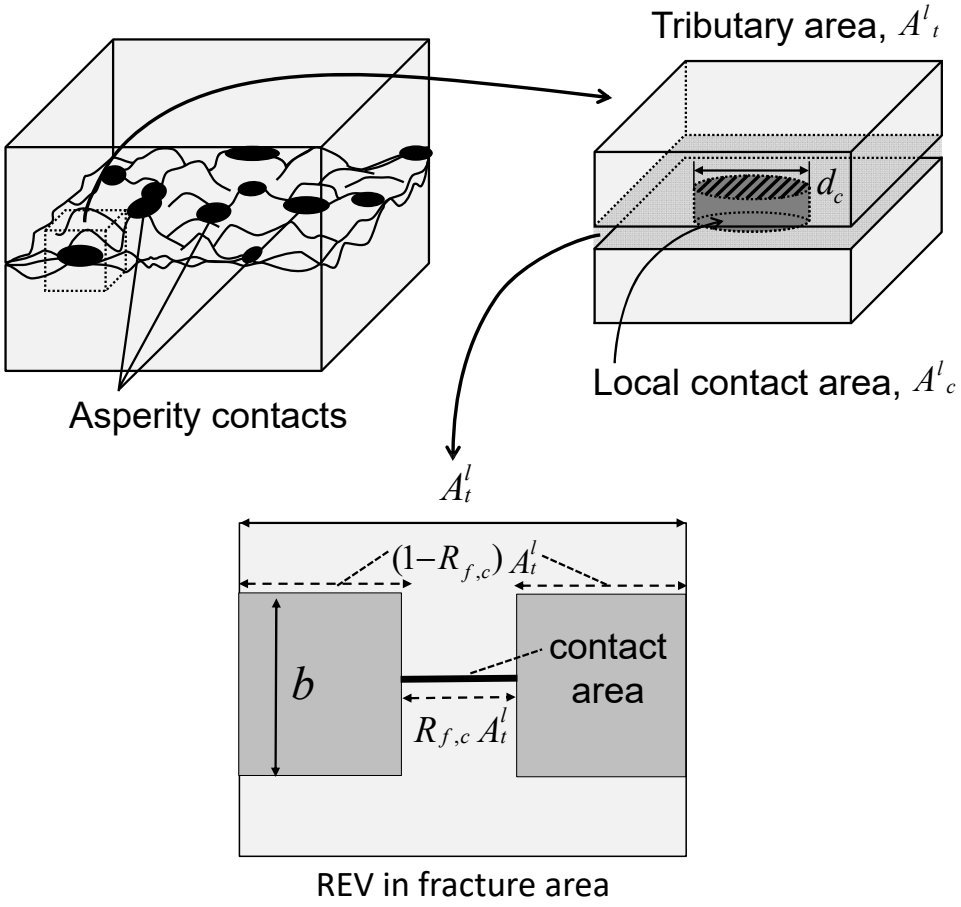

Fig. 3 Geometrical model that includes representative element in rock fracture area [13].

760

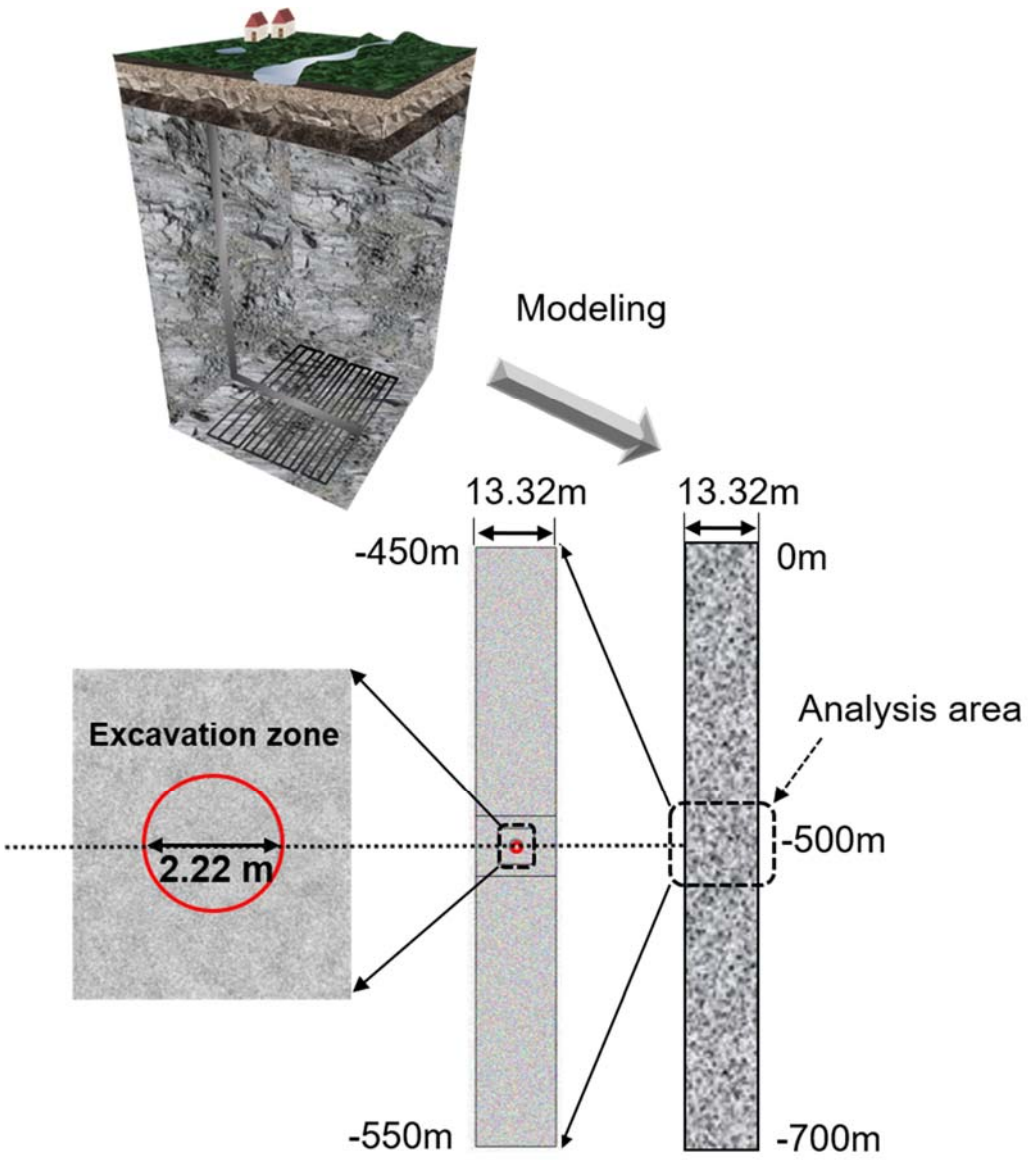

761

762 **Fig. 4** Numerical domain for long-term simulations.

763

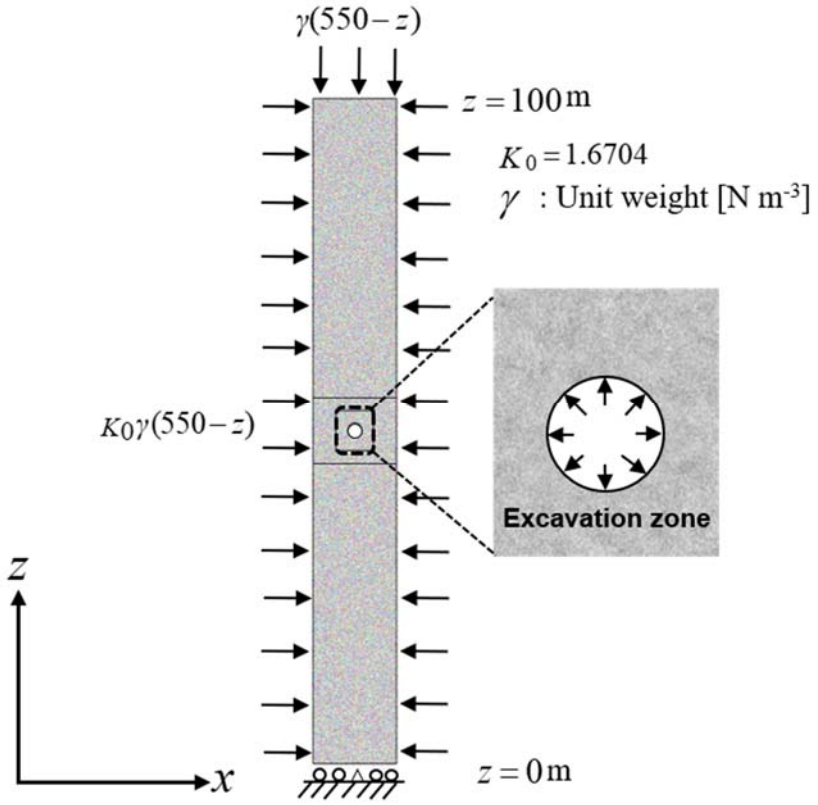

764

765 **Fig. 5** Description of excavation analysis.

766

767

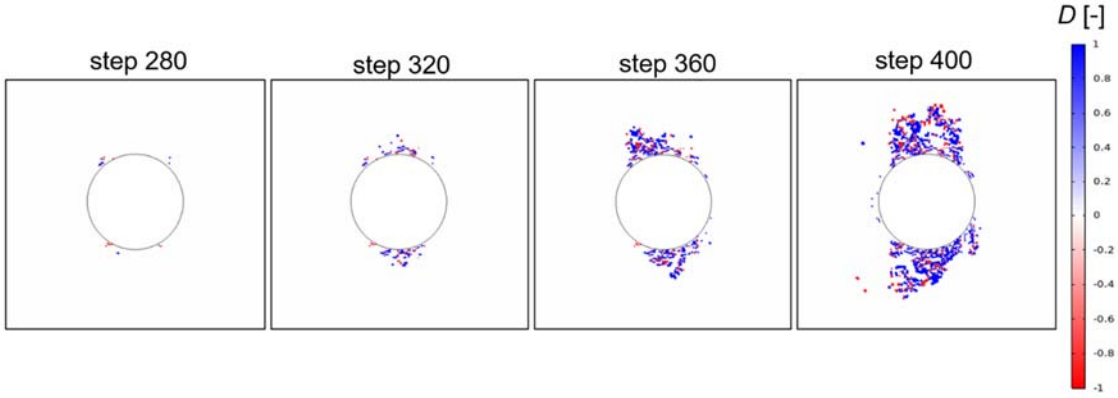

768

769 **Fig. 6** Evolution of damaged zone during cavity excavation.

770

771

772

773

774

775

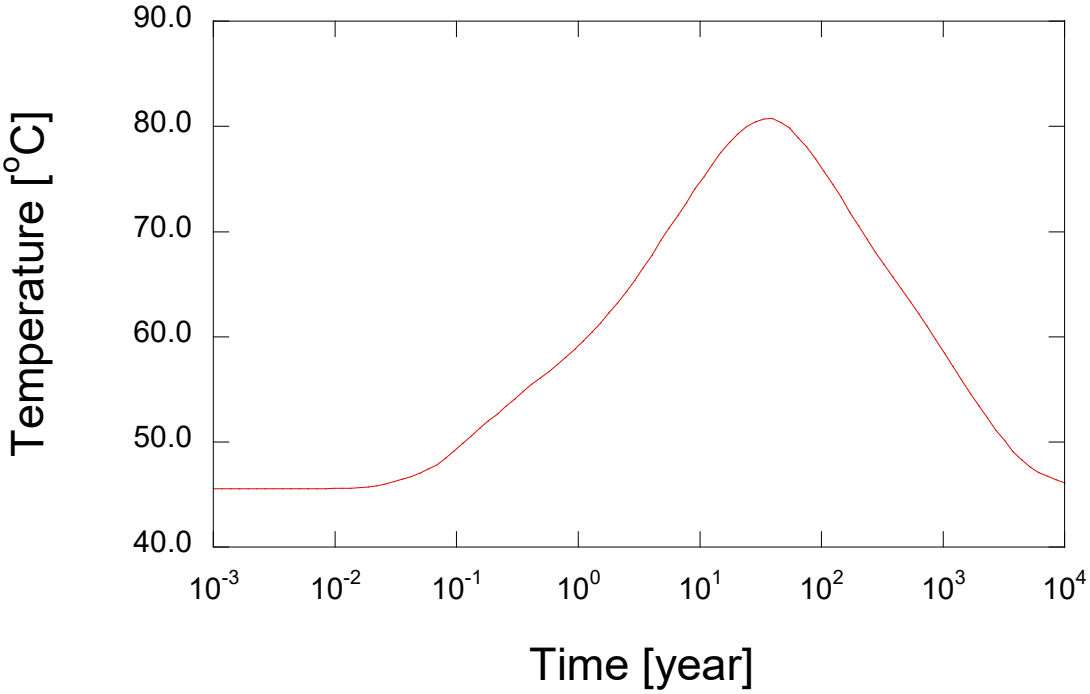

Fig. 7 Temperature depending on time T_b (t) set as boundary condition at periphery of cavity [1].

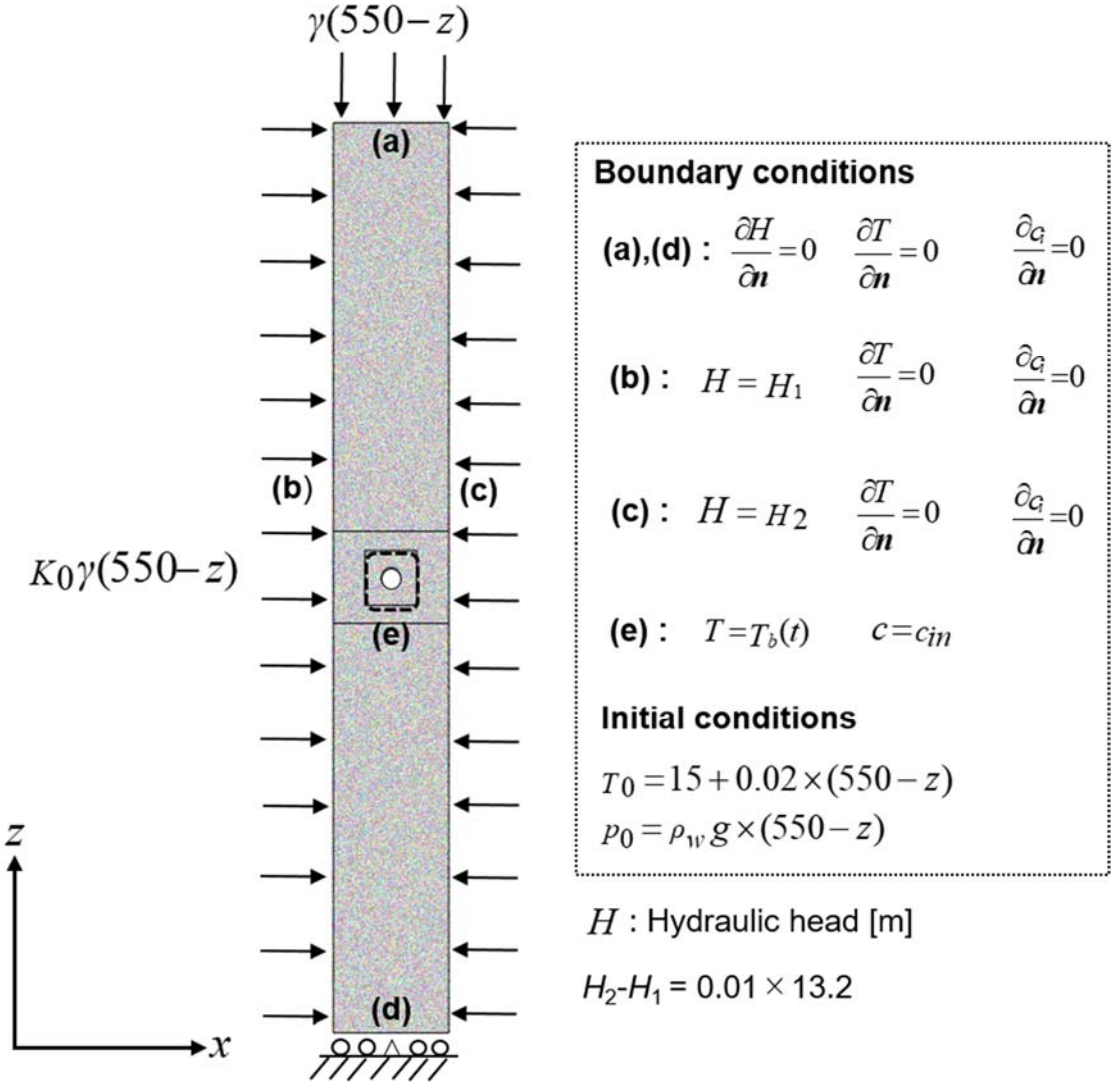

Fig. 8 Boundary conditions of long-term coupled THMC simulations.

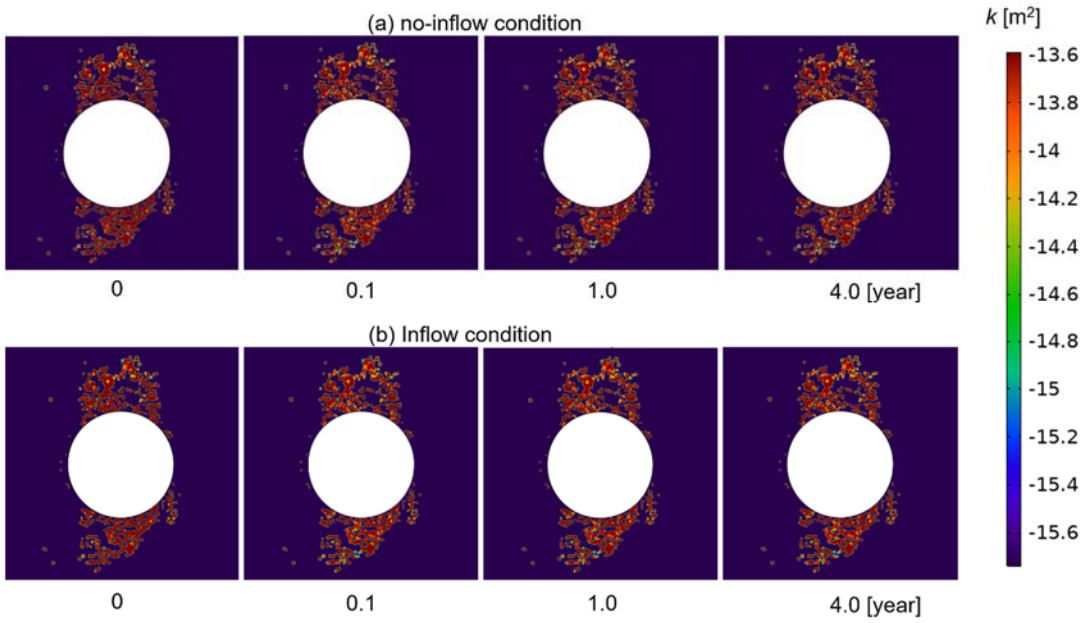

Fig. 9 Change in permeability distribution around cavity with time in range of 0 – 4.0 years under (a) no-inflow condition and (b) inflow condition

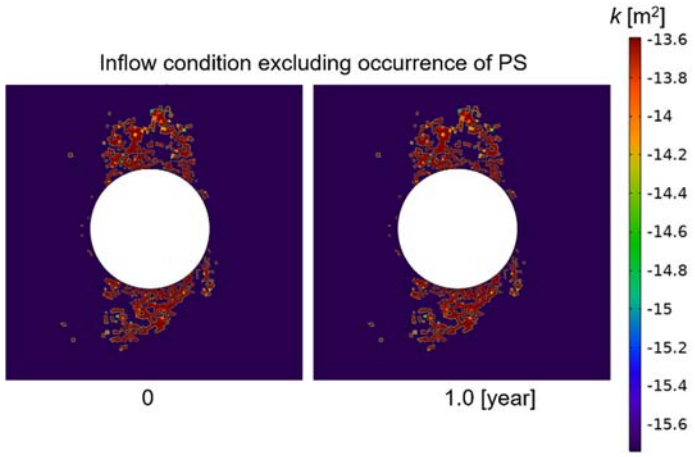

Fig. 10 Permeability distributions around cavity at initial state and after 1.0 years in case considering inflow condition, which does not consider occurrence of pressure solution.

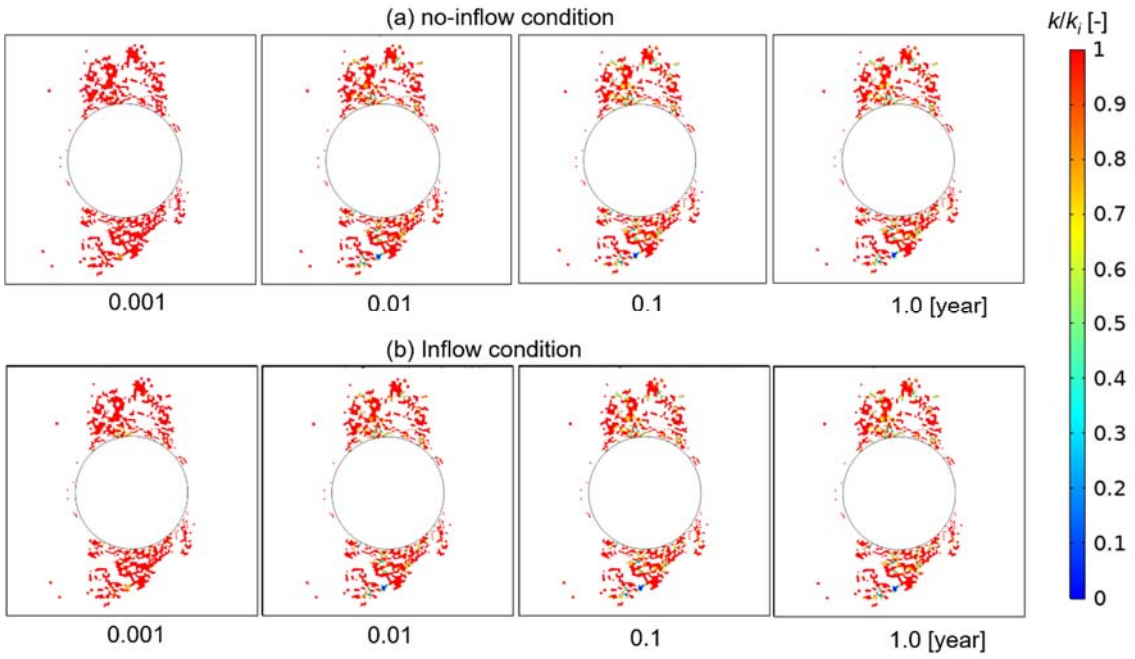

Fig. 11 Change in normalized permeability distribution around cavity with time in range of 10^{-3}–1.0 years under (a) no-inflow condition and (b) inflow condition.

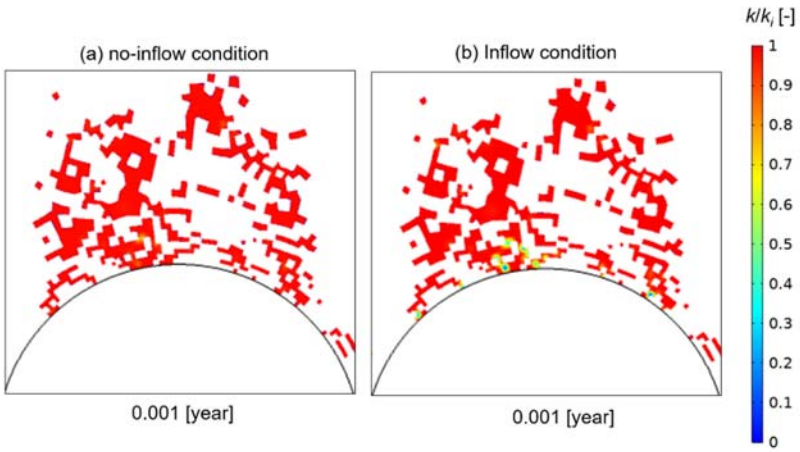

Fig. 12 Normalized permeability distributions focused near the invert at 0.001 years after disposal of waste package under (a) no-inflow condition and (b) inflow condition.

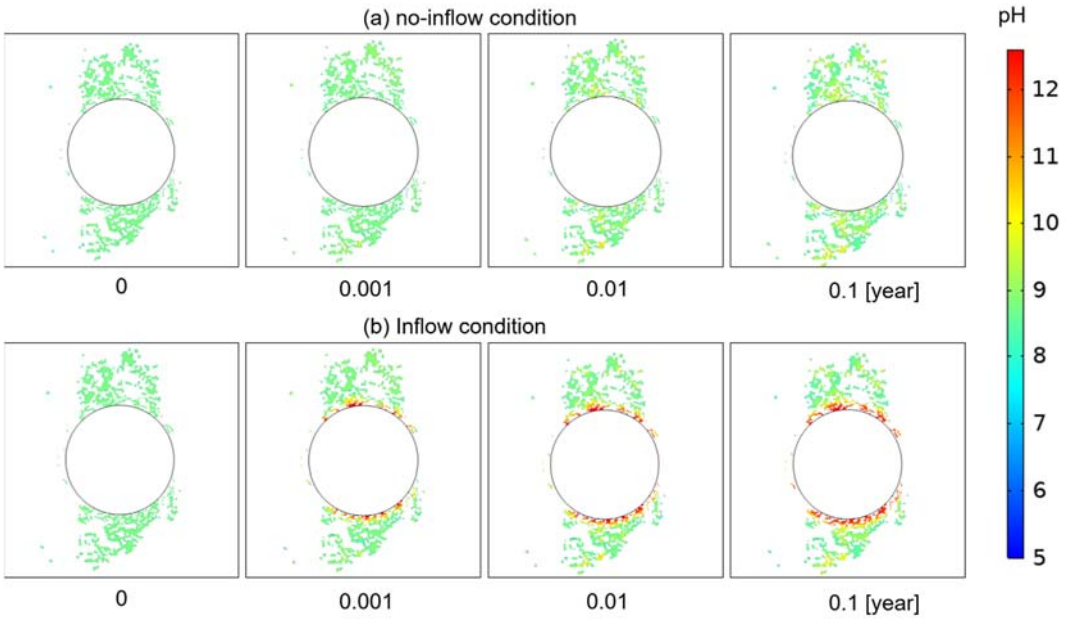

Fig. 13 Change in pH distribution within fracture with time in range of 0 – 0.1 years under (a) no-inflow condition and (b) inflow condition

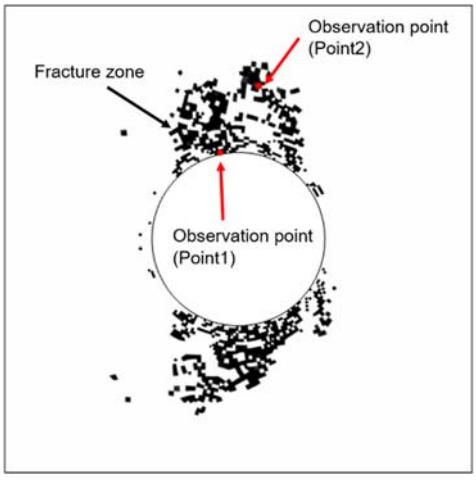

Fig. 14 Setting observation point. Points1 and 2 are set in the computed fracture zone where permeability reduction with time occurs. Point1 is set in the vicinity of the cavity and Point2 is set in a place a little away from the cavity.

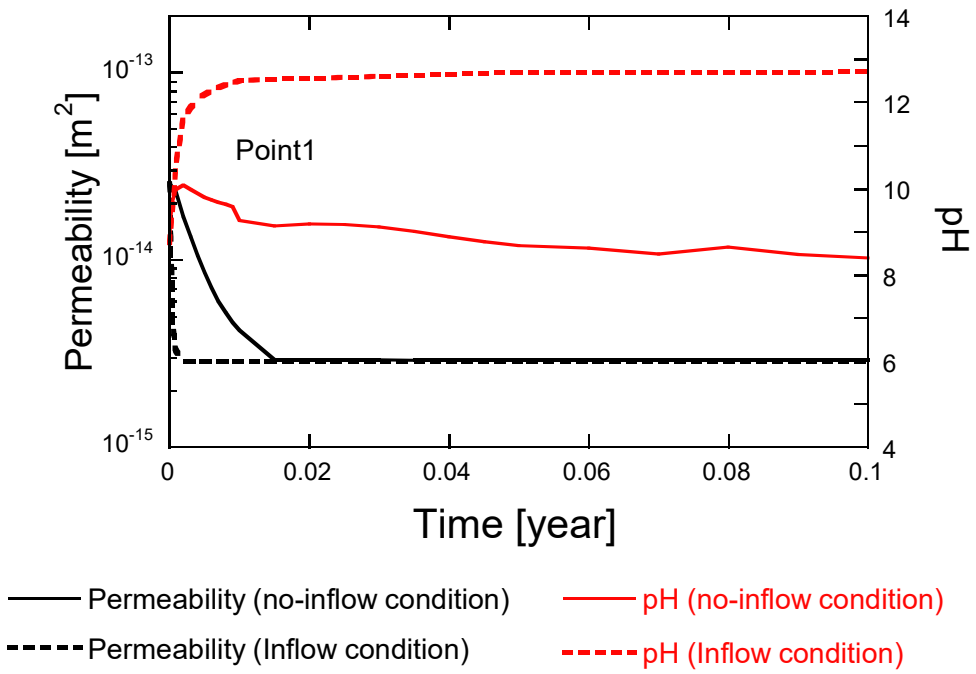

838

839 **Fig. 15** Changes in permeability and pH within first 0.1 years under no-inflow condition and inflow
840 condition at observation point (point 1) in fracture zone depicted in **Fig. 14**.

841

842

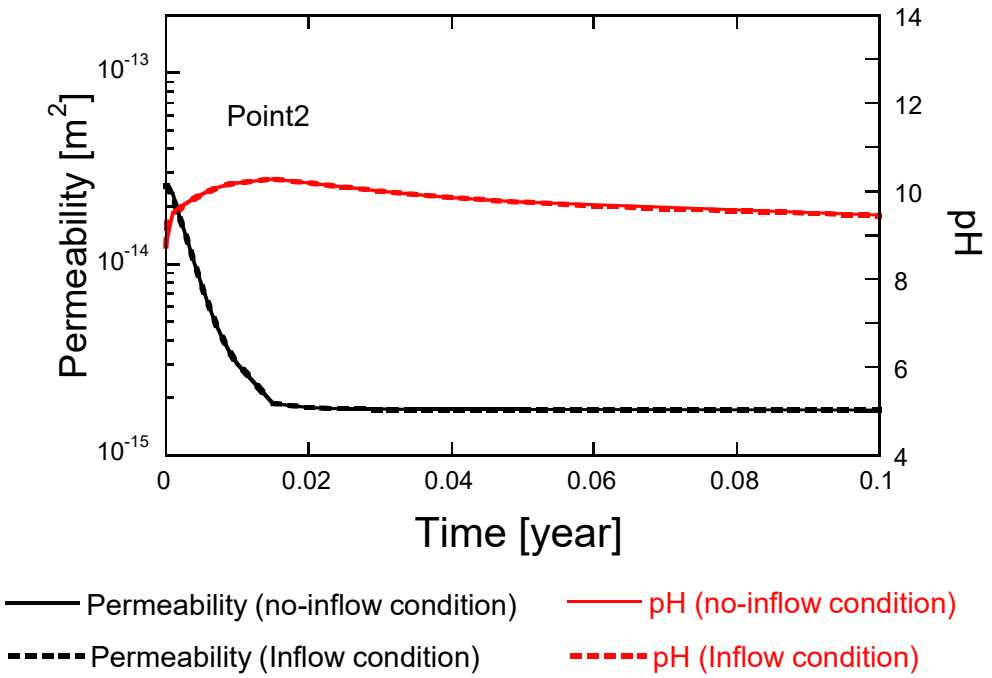

843

844 **Fig. 16** Changes in permeability and pH within first 0.1 years under no-inflow condition and inflow
845 condition at observation point (point 2) in fracture zone depicted in **Fig. 14**.

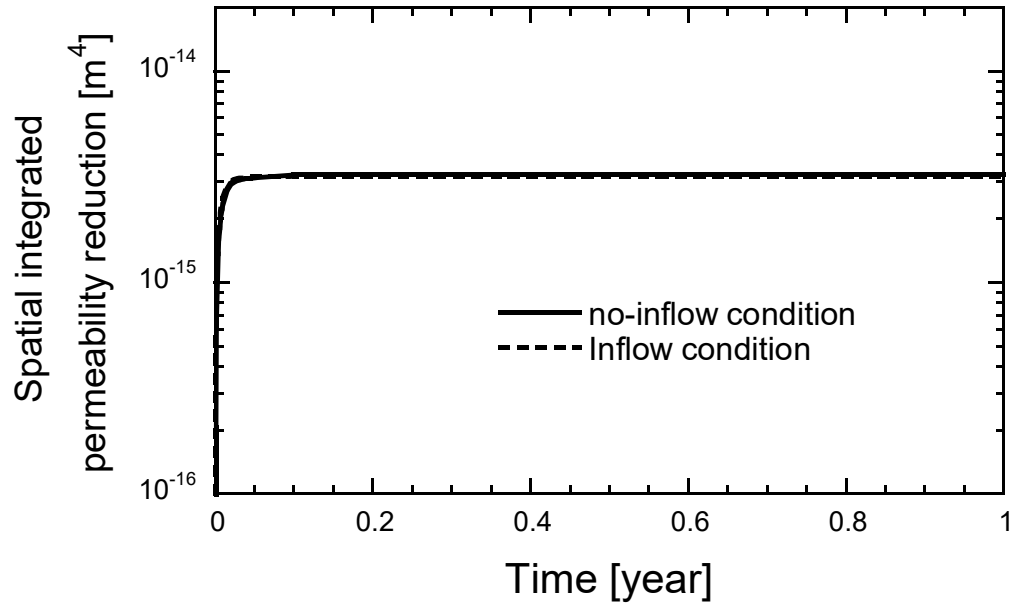

Fig. 17 Changes in space integrated permeability reduction within 1.0 years under no-inflow condition and inflow condition.

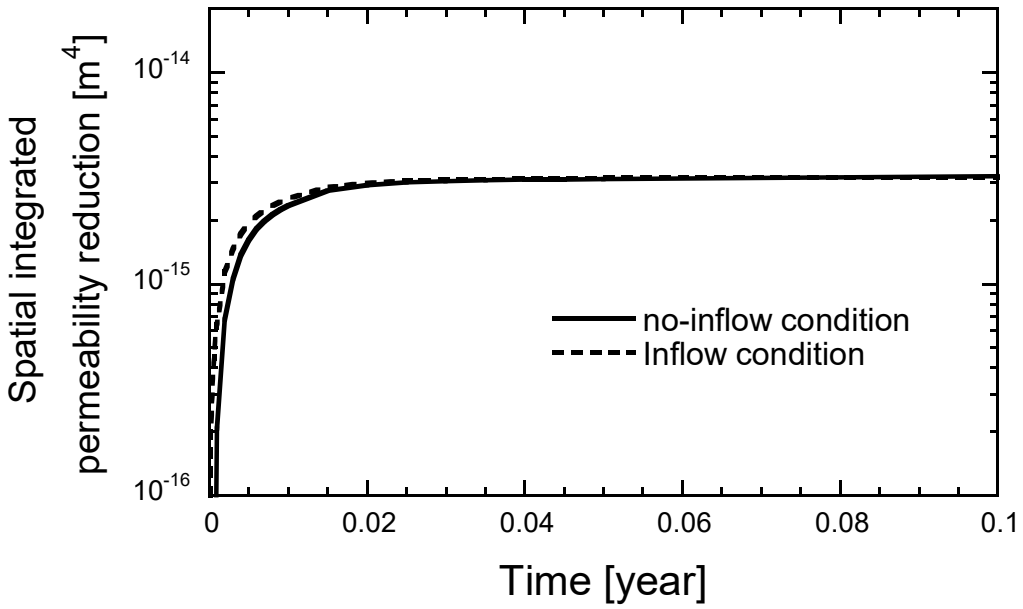

Fig. 18 Changes in space integrated permeability reduction within first 0.1 years under no-inflow condition and inflow condition.